Maryami, R., Azarpeyvand, M., Dehghan, A. A., & Afshari, A. (2019). An Experimental Investigation of the Surface Pressure Fluctuations for Round Cylinders. *Journal of Fluids Engineering*, *141*(6), [061203]. https://doi.org/10.1115/1.4042036

An experimental investigation of the surface pressure fluctuations for round cylinders

R. Maryami[1]
e-mail: r.maryami@gmail.com
Yazd University, Yazd, Iran

M. Azarpeyvand[2]
e-mail: m.azarpeyvand@bristol.ac.uk
University of Bristol, Bristol, United Kingdom, BS8 1TR

A. A. Dehghan[3]
e-mail: adehghan@yazd.ac.ir
Yazd University, Yazd, Iran

A. Afshari[4]
e-mail: afshar.abbas@gmail.com
Yazd University, Yazd, Iran

ABSTRACT

An experimental study is carried out to investigate the unsteady pressure exerted on the surface of a round cylinder in the subcritical Reynolds number range. Results are presented for the surface pressure fluctuations, spanwise coherence, lateral correlation length and peripheral coherence. Discussions are provided for the dominance of the first three vortex shedding tones at different regions of the cylinder and the size of the flow structures around the cylinder. The dataset provided have shed new light on the unsteady aerodynamic loading acting on cylinders and provides the impetus for further research on the aerodynamics and aeroacoustics of bluff bodies.

Keywords: *Circular cylinder, surface pressure fluctuations, Aeolian tone, vortex shedding*

1. INTRODUCTION

The aerodynamics of circular cylinders placed in a laminar cross-flow has extensively been studied as it involves some very interesting physics and is of great importance in many engineering applications, including risers in marine engineering, buildings, bridges, tubular heat exchangers, power

[1] School of Mechanical Engineering, Yazd University, PhD student
[2] Department of Mechanical Engineering, University of Bristol, Senior Lecturer and Royal Academy of Engineering research fellow
[3] School of Mechanical Engineering, Yazd University, Associate Professor
[4] School of Mechanical Engineering, Yazd University, PhD student

transmission lines, chimneys, towers and so on. The noise generation mechanism and methods to reduce the noise from bluff bodies are also of great academic and industrial interest. While the aerodynamics of bluff bodies has been the subject of much experimental studies, there still exists a need for high-quality measurement of the quantities important for the understanding of the noise generation mechanism.

The broadband and tonal characteristics of the noise generated by circular cylinders depend on the Reynolds number of the flow [1]. At the Reynolds numbers below 50, the separation of the boundary layer on the cylinder causes a pair of vortices, but no shedding behind the cylinder. Within the Reynolds number range of 50 to 10^5, known as the subcritical flow regime, the boundary layer over the cylinder remains laminar, but periodic shedding of vortices occur in the wake region. At higher Reynolds numbers, the boundary layer becomes turbulent, followed by flow separation, leading to strong random flow fluctuations as well as the emergence of period shedding structures in the wake region. A complete review of the different flow regimes, vortex shedding structures and the Reynolds number dependency of the vortex shedding phenomenon can be found in [2].

The sound generated as a result of the flow interaction with circular cylinders can be characterized as both tonal, due to the period aerodynamic forces acting on the cylinder due the vortex shedding, and broadband, because of the presence of strong three-dimensional random fluctuations within the boundary layer and the near-wake. The sound generation due to the vortex shedding has received considerable attention since the pioneering research of Strouhal [3] in 1878, who made the first quantitative measurement of the sound generated from air-flow over stretched wires. Strouhal's measurements showed that the frequency of the tonal noise produced as a result of flow interaction with the wires is independent of the wire length and that it can be described using a non-dimensional frequency relationship, now known as the Strouhal number ($St = fD/U_\infty$). The wake measurements for round cylinders von Karman [4] also confirmed the emergence of such tones. These experimental observations, in conjunction with some flow stability analysis [4], led to the association of the flow

induced tones to the periodic vortex shedding within the wake region of the cylinder [5]. Rayleigh also showed that the vortex shedding Strouhal number is a function of Reynolds number. The Reynolds number dependency of the radiated tonal noise or vortex shedding frequency was further confirmed by later experiments [6]. Other experimental studies in the low Reynolds number regime have shown the emergence of periodic vortex shedding structures at a Reynolds number of 40 [7] and appearance of more three-dimensional irregular and turbulent structures for $Re \geq 300$ [8].

The Aeolian tones, i.e. the tonal noise generated due to the vortex shedding, are known is a basic and important characteristic of the aerodynamic of bluff bodies. Stowell and Doming [6] were the first to measure the directivity of the noise radiated by circular cylinders and demonstrated that the sound field has a dipolar character, with peaks normal to the freestream flow direction and the cylinder axis. The mathematical model developed by Curle [9] showed that the fluctuating forces acting on the cylinder, as a result of the solid-flow interaction, leads to a dipolar radiation. Curle's dimensional analysis also showed that theoretically the sound intensity scales with the sixth-power of the velocity. The experimental work Yudin [10], however, found that the sound power scaling law can vary significantly with flow condition and Reynolds number.

The prediction of the sound radiated by an isolated cylinder in a crossflow has been the subject of many studies over the past few decades, a summary of which can be found in the work by Blevins [11]. Assuming an acoustical dipole in a moving medium and by modelling the vortex shedding as an externally exerted body force, Etkin and Keefe developed a model for the prediction of the radiated noise [12]. Lighthill's Acoustic Analogy has also been extended by Curle [9] and Ffowcs Williams and Hawkings [13] to allow for the effects of external solid bodies and their motion, respectively. Based on the mathematical models developed, it has become evident that the far-field noise can be predicted using some of the flow quantities, namely the vortex shedding frequency, the aerodynamic loading acting on the cylinder, and the spanwise correlation length of the flow structures as a function of

frequency. While the aerodynamic loading, i.e. lift and drag response, shows the strength of the oscillation and therefore the noise radiation, the spanwise correlation length represents the three-dimensional character of the flow and the coherence level of the flow structure, particularly at the vortex shedding frequency and it harmonics.

Based on Curle's mathematical model for the prediction of noise from stationary solid bodies in a flow, one can infer that the far-field sound from a circular cylinder is directly related to the surface integral of the unsteady pressure exerted on the body of the cylinder as a result of the interaction with the boundary layer and wake structures [14]. Therefore, for proper understanding of the noise generation mechanism from external bodies in a flow, it is important to study the flow-field around the object and the unsteady forces exerted by flow structures. The most conventional and effective method for measuring the unsteady surface pressure fluctuations acting on the surface in a flow field is the use of miniature pressure transducers. Using such a method, one can obtain reliable measurement of the unsteady pressure over a wide range of frequencies. A potential shortcoming of the method, on the other hand, is that the spatial resolution, i.e. the distance between the transducers, is restricted to the physical size of the transducers. This can cause problems with pressure coherence studies and resolving high-frequency structures. A comprehensive study of vortex shedding noise from a single cylinder using this method was carried out by Schlinker et al. [15]. Results had confirmed that vortex shedding is dependent on the surface roughness and the effective Reynolds number. It was also shown that the vortex shedding noise is particularly strong in the subcritical Reynolds number range and that in the supercritical regime the far-field noise becomes more broadband. The wall pressure fluctuation measurements using in-situ pressure transducers were also reported in the work by Casalino and Jacob [16] for understanding of the statistical characteristics of the wake flow structures. Two-point coherence measurements were also performed using a limited number of angular and spanwise pressure sensors. In this research, the Aeolian tones were detected at each observation angle corresponding to the typical

Strouhal number of 0.2. It was also argued that both the fundamental vortex shedding frequency and the second harmonic correspond to the lift fluctuations of the cylinder, while the first harmonic is related to the drag fluctuation force acting on the cylinder. Using the same measurement technique, Fujita et al. [17] carried out an investigation on the properties of the Aeolian tone and the surface pressure fluctuations for a wide range of Reynolds numbers between 2.5×10^5 and 2×10^6. According to the experimental data obtained in [17], the wake flow experiences significant changes at $Re = 3 \times 10^5$, leading to sudden increase in the Strouhal number of the Aeolian tone from 0.2 to 0.45. The Strouhal number of the Aeolian tones were found to remain at around 0.45 up to $Re = 7.5 \times 10^5$, followed by a decrease to 0.2 at higher Reynolds numbers. The spanwise correlation studies between the surface pressure fluctuation and the Aeolian tones had also shown that in the sub-critical range, the vortex shedding structures are more two-dimensional than those in the super-critical flow range.

In addition to the conventional methods, such as the miniature pressure transducers, for the measurement of the surface pressure fluctuations, new non-intrusive methods based particle image velocimetry (PIV) has opened a new field of research. The pressure field can be extracted from the PIV velocity field and used in the context of aerodynamic noise diagnosis. Such PIV-based methods have recently been used for some fundamental problems, such as the flow over circular cylinders [14]. The noise sources were then identified and assessed through cross-correlation analysis of the pressure fluctuations. The pressure field results obtained using the PIV method had shown that the noise sources can be found mainly at the flow separation point on the cylinder and within the near-wake region. The pressure field obtained based on the PIV method was also found to be in good agreement with that measured using an embedded pressure transducer. The PIV technique has also been widely used for studying flow control around circular cylinder using permeable plates and porous covers [18, 19].

As reviewed above, there exists an extensive body of research on the generation of aerodynamic noise from cylinders and the prediction of the radiated noise. However, no comprehensive study has

been carried out to investigate the surface pressure fluctuations over the circumference of the cylinder and along its span. This paper aims to provide an extensive study of the unsteady pressure exerted on the surface of circular cylinders in a laminar cross-flow in the subcritical flow regime, perform comprehensive near-field correlation studies and improve our understanding of the noise generation mechanisms from bluff bodies. We will make use of in-situ unsteady pressure measurements and will provide a large database, which can be used both for better understanding of the noise generation and as a benchmark case for future numerical studies. The remainder of the paper is organized as follows: Section 2 describes the test-rig, model instrumentation and data processing methods. Section 3 details the experimental data collected as part of this research work and provides discussions on the surface pressure fluctuations, spanwise coherences, correlations lengths, and peripheral coherence analysis. Finally, Section 4 concludes the paper and provides suggestions for future research.

2. EXPERIMENTAL SETUP

The Experiments were performed in an open-jet subsonic wind tunnel with an exit cross-sectional area of $460\ mm \times 460\ mm$. A low-noise forward-blade type centrifugal fan powers the wind tunnel, providing a maximum reliable wind speed of 25 m/s, with an incoming turbulence level of less than 0.3%. To further improve the noise performance of the tunnel and avoid noise contamination due to the fan background noise, the internal walls of the tunnel were replaced with a highly absorbing porous layer [20], which resulted in the reduction of the fan background noise by about 15 dB over a wide range of frequencies.

2.1. Test Model

The cylinder model tested in the present work has an outer diameter of 22mm and a span length of 460mm. In order to simplify the instrumentation of the model with in-situ pressure sensors, the circular

cylinder model is made of three parts, namely one middle section with the static and dynamic pressure instrumentations and two side parts to extend the span length of the model to that of the wind tunnel exit, as shown in Fig. 1. The blockage ratio of the test rig is less than 5%. The model also has an aspect ratio (span-length to diameter) of over 20 and therefore the wind tunnel walls effects on the measured quantities can be assumed negligible [21]. The cylinder is placed within the potential core of the exiting jet flow and supported by two parallel rectangular end-plates downstream of the contraction nozzle. The model is properly fixed to the side-plates to eliminate the possibility of vibration. The cylinder is mounted on a turning-table to enable data collection using the static pressure taps and pressure transducers in fine angular increments. The details of the experimental setup are provided in Fig. 1.

2.2. Static Pressure Measurement

In order to study the cylinder flow-field and measure the pressure distribution around the cylinder (C_p), the model is instrumented with 18 static pressure taps, distributed evenly with 20° spacing over the circumference of the cylinder, as shown in Fig. 1. The pressure taps have a diameter of 0.55 mm. Each tap-hole is tightly fitted with a 5 mm long brass tube, with the inner and outer diameters of 0.4 mm and 0.6 mm, respectively. The brass tubes are then connected to a series of polyurethane tubes with the diameters of 1mm, 3 mm and 4 mm, and finally connected to the pressure scanner ports outside the cylinder. The static pressure measurements are carried out using a Honeywell electronic differential pressure measurement unit with 16 channels and a range of ± 1.25 kPa. An uncertainty analysis of the pressure measurement, based on the method described in [22], showed a maximum uncertainty of 2.2%. As mentioned above, while the pressure taps are spaced at every 20°, the cylinder can be rotated in 5° increments using the turning-table, providing the possibility of pressure measurement with fine angle (θ) resolution.

2.3. Surface Pressure Microphone Array

The layout of the pressure transducers used for the measurement of the dynamic pressure acting on the surface of the cylinder is depicted in Fig. 1. The locations of the pinholes are also summarized in Table 1. A total number of 15 microphones are distributed in the spanwise and peripheral directions. A set of microphones (p1-p8) are installed on a straight line along the span of the cylinder to verify the two-dimensionality of the flow and also to measure the spanwise length-scale at different frequencies. Special care has been taken for the distribution of the spanwise pressure transducers. To fully resolve the flow structures, the spanwise transducers must be distributed over at least 5D-7D, as reported in the literature [17, 23, 24]. At the same time, the transducers must be kept outside the boundary layer developed by the wind tunnel side-plates. The maximum thickness of the boundary layer created on the side-plates at the flow velocity of 20m/s is found to be 8 mm. In this study, the pressure transducers are distributed over 6D (132 mm) along the span and are always outside the side-plate boundary layer. The minimum distance between the transducers is limited by the physical dimension of the transducers. The pressure transducers are distributed along the span of the cylinder according to a potential function, with an unequal spacing. This is to provide a non-redundant population of sensor spacing, maximum number of spatial distance combinations and therefore more accurate cross-correlation and spanwise length-scale calculations. Another set of pressure transducers (p9-p15) are distributed around the circumference of the model at the mid-span plane with an angular spacing of 45°, to provide information on the flow structures and shedding at different peripheral angles. The turning-table has been used to collect data at every 5° degrees.

2.4. Surface Pressure Instrumentation

Unsteady surface pressure measurements are made using Panasonic electret condenser pressure transducers (series WM-61A). The transducers have a diameter of 2.5mm, height of 3.4 mm and circular sensing area of 2 mm. The same type of pressure transducers had previously been used in

similar studies [23] and has shown to deliver reliable pressure recording in the frequency range relevant to the current study. The accurate measurement of the dynamic pressure due to the flow interacting with the cylinder requires the use of extremely small pressure transducers. This is, however, not possible in practice. At low frequencies, when the sensing area of the pressure transducers is smaller than the sound or hydrodynamic field wavelength, accurate pressure measurements can be achieved. At high frequencies, on the other hand, when the wavelength is smaller than the pressure transducer sensing area, the pressure fluctuation measurement is spatially integrated, leading to inaccurate measurement of the dynamic pressure, as reported in [25, 26]. In order to reduce the attenuation effects at high frequencies, pressure measurements are made via a small pinhole at the surface of the cylinder. Also, as reported by Bull and Thomas [27] and Afshari et al. [28], the discontinuity on the surface of the model due to the presence of the pinholes can cause flow disturbance and errors in the measurement at high frequencies. Such errors can be minimized to a large extent by employing pinholes with very small diameters [29].

As shown in Fig. 2, the pressure transducers are placed inside the cylinder, underneath a small pinhole mask of 0.55 mm diameter, and fixed in place using a fully sealed holding mechanism. The pinholes are made using an accurate drill machine. The geometrical dimensions of the pinholes and the pressure transducer holding mechanism are shown in Fig. 2. Moreover, the cavity between the pressure transducer and the pinhole mask can cause cavity resonance, which is an undesirable consequence of such in-situ measurement techniques. The most important parameters determining the cavity resonance frequencies for the pinhole configuration are the pinhole diameter, pinhole neck length and volume between the microphone and the mask surface [30]. Analytical and experimental investigations have been carried out as part of our test-rig design and manufacturing to ensure that the resonance frequencies associated with the pinhole configuration are outside our frequency range of interest, i.e. up to 20 kHz.

The microphone calibration was performed before each test in the following manner. In order to acquire the transfer function of the pressure transducers a purpose-built calibrator was used. A bespoke calibrator was designed and made as part of this research, consisting of a high-quality loudspeaker, connected to a cone-shaped extension with a 110mm long tube with a diameter of 10 mm, microphone chamber, and an acoustic termination see Fig. 3. The cone was designed with a shallow angle and filled with a dense porous material to ensure plane wave propagation and suppression of high-order modes. An extension tube connects the cone to the microphone chamber, with a microphone holder that aligns the reference microphone to the pinhole of the embedded pressure sensor. In order to ensure the proper sealing during the calibration, the area around the pinhole is covered by a thin silicone ring during the calibration process. A ¼-inch 40BP GRAS microphone, calibrated with a GRAS Sound Calibrator (Type 42AB), was used as the reference microphone. A long and very highly absorptive plastic tube is also used for the termination of the sound field from the microphone chamber and suppression of reflected waves. All pressure sensors installed in the test rig were calibrated in-situ with a white noise excitation signal over the frequency range of 10 Hz to 20 kHz. A 16-channel power module was used to power the Panasonic pressure transducers and the data were collected using a 16-channel NI PCI-6023E data acquisition system. The pressure data have been collected over 20 seconds at a sampling frequency of $f_s = 40$ kHz. Figure 4 shows the amplitude and phase of the transfer function for one of the embedded Panasonic pressure transducers in the pinhole configuration. As shown, the microphone delivers a linear and smooth response at all frequencies and the pinhole cavity does not produce any resonances within the frequency range of interest (100-10kHz). The main source of uncertainty in the measurement of the unsteady surface pressure here is due to the statistical convergence error, and is inversely proportional to the number of sample records [31], i.e. $1/\sqrt{N_r}$, with N_r being the number of records. In the present study, the spectra have been calculated as the average of the spectra of individual data records obtained from dividing the pressure time series into a sequence of records to reduce the

statistical convergence error. A total number of $N_r = 800$ records have been used, resulting in an uncertainty of about 3.5%.

3. RESULTS AND DISCUSSIONS

3.1. Aerodynamic Characteristics

The results of the pressure distribution around the cylinder model are presented in this section. The results here also serve as the validation of the experimental setup and wind tunnel used for the present study. The experiments were carried out at three different freestream velocities, $U_\infty = 10, 15$, and 20 m/s, corresponding to the Reynolds numbers of $Re = 14.7 \times 10^3,\ 22 \times 10^3$ and 30×10^3, respectively, based on the diameter of cylinder. This Reynolds number range is limited to subcritical regime, as reported by Zdravkovich [2]. Figure 5 compares the data measured as part of our experimental campaign against some other experimental data available in the literature with similar flow condition. It is well recognized that the pressure coefficient can be greatly affected by the wind tunnel blockage ratio (B) and the cylinder span-length to diameter ratio [32]. To show the validity of the current measured data, results have been comp`1ared against those from previous works with similar blockage ratios (Weidman [33], Fage and Falkner [34], Sade and Sharon [35], Sun et al. [36] and Gu et al. [37]). The pressure results are presented only for the top side of the model ($\theta = 0^\circ - 180^\circ$). As shown in the figure, the pressure distribution is almost independent of the Reynolds number in the subcritical flow regime, which is consistent with the results in the literature [2]. The comparison has also shown that our measured data is in good overall agreement with those in the literature. The pressure coefficient minimum occurs at the angular position $\theta_m = 70°$ and the base region, i.e. the region of nearly constant pressure, extends from $\theta = 80^\circ$ to 180° at all Reynolds numbers, consistent with the values reported in [33-37]. In the base region, the deviation of the pressure coefficient with respect to the base pressure coefficient C_{P_b} (i.e. pressure coefficient at $\theta_b = 180°$) is approximately 3%, which is

similar to the base pressure values reported in [33, 34]. In the present study, the skin friction was not measured since in the subcritical regime the friction drag is negligible compared to the total drag. Therefore, the separation angle θ_s (i.e. the angle at which skin friction is zero and in considered as the beginning of the base region [34]) is estimated using the pressure coefficient distribution and is found to be about 80° for the three subcritical Reynolds numbers considered in this study.

3.2. Pressure Power Spectral Density

The surface pressure power spectral density (PSD) has been measured using microphone p1 at several peripheral angles, at $Re = 30 \times 10^3$. The surface pressure PSD results are presented in both line-plot and contour-map formats in Fig. 6 as a function of the Strouhal number. The PSD calculations are performed in Matlab using the Pwelch function. Hamming windowing with 50% overlap is applied to obtain smoother and more accurate results. The frequency resolution was set to 64 Hz. The pressure PSD data are referenced to 20 μPa. The PSD results are presented only when the surface pressure fluctuations are at least 10dB higher than the background noise due to the freestream flow. In addition to the fundamental vortex shedding frequency ($St \approx 0.2$), the first four harmonics are also visible in the PSD results, thanks to the good signal to the background noise ratio. For the pre-separation angles ($\theta \leq \theta_s$), results show that both the broadband and tonal content of the PSD spectra increase with the angle. The increase in the broadband energy content can be due to the increase in the boundary layer thickness and emergence of larger flow structures, while the increase at the tonal frequencies is due to its distance from the vortex shedding region. For the post-separation locations ($\theta > \theta_s$), the tonal frequencies are found to have a very high energy level, protruding well above the broadband part of the surface pressure spectra. It can also be seen that the broadband energy content of the pressure spectra generally increases with the angle. An interesting observation here is that at $\theta = 180°$, the fundamental frequency disappears, and the 1st harmonic ($f_1 = 2f_0$) remains as the only noticeable tonal peak. The

disappearance of the fundamental tone will be further discussed later in Section 3.3. One can also see from the results that the slope of the surface pressure PSD changes greatly with frequency and angle. At small angles and low frequencies, the PSD spectra are dominated by the tonal peaks and it is not easy to find a slope for the broadband content of the surface pressure energy field. At larger angles, particularly beyond the separation point, the broadband content of the surface pressure PSD begins to increase and follows certain f^{-n} decay gradients. At large angles ($\theta > 135^o$), and particularly at the cylinder base ($\theta = 180^o$), the surface pressure PSD spectra follow a gradient of about f^{-1} within $0.1 < St < 0.4$, $f^{-1.5}$ after the 1st harmonic (f_1) and f^{-3} at very high frequencies ($St > 6$).

In order to gain a better understanding of the surface pressure PSD variation with the angle, the amplitude of the fundamental vortex shedding frequency and its first and second harmonics (f_1 and f_2), are extracted from the data Fig. 6 and presented in Fig. 7. The results show that the amplitude of the fundamental peak (f_0) increases with the angular position of the pressure transducers between $\theta = 0° - 75°$. The f_0-amplitude remains nearly constant within $75° < \theta \leq 105°$ and then decreases for $\theta > 105°$. At $\theta = 180°$, the fundamental tone disappears completely, shown as the hollow circles in the figure, which are simply the values of the broadband noise at $St = 0.2$. The same trend can be observed for the peak values of the 2nd harmonic ($f_2 = 3f_0$), although in this case the tones disappear for angles $\theta > 135°$, presented as the hollow triangle markers. For the 1st harmonic ($f_1 = 2f_0$), the magnitude of the tone increases uniformly from $\theta = 0°$ to 180°, with two small plateau regions between $0° < \theta \leq 20°$ and $40° < \theta \leq 90°$. Results also show that both the f_0 and f_2 tones peak at around $\theta = 80°$, while that for f_1 occurs at $\theta = 180°$. This indicates that the fundamental and 2nd harmonic reach their peak values near the separation point, while the 1st harmonic continues to grow into the fully separated flow and peaks at the cylinder base ($\theta = 180°$). These observations are consistent with the general understanding of the unsteady aerodynamic loads acting on isolated cylinders and that the odd ($f_0, 3f_0, \ldots$) and even ($2f_0, 4f_0, \ldots$) harmonics correspond to the cylinder unsteady lift and drag

fluctuations, receptively [16]. It is well known that the axial oscillation frequency of a cylinder, due to the unsteady drag force, is twice the vertical oscillation frequency, due to the unsteady lift force, but the amplitude of the vertical fluctuating forces are often larger than the forces in the streamwise direction [16]. These observations are particularly important for the better understanding of the noise generation mechanism from bluff bodies.

3.3. Lateral and Azimuthal Coherence

3.3.1. Lateral Coherence

The results in the previous section showed the changes to the surface pressure PSD and the vortex shedding frequencies at different peripheral angles. In this section, we shall investigate the changes to the shape of the flow structures by studying the spanwise and azimuthal coherences between different pressure transducers. The measurement of coherence can help gain a better understanding of the physical size and also lifespan of flow structures. The coherence between two pressure transducers along the span can be defined as:

$$\gamma^2_{p_i,p_j}(\eta_z,f) = \frac{\left|\Phi_{p_i,p_j}(\eta_z,f)\right|^2}{\Phi_{p_i,p_i}(\eta_z,f)\Phi_{p_j,p_j}(\eta_z,f)} \quad (1)$$

where $\Phi_{p_i,p_j}(\eta_z,f)$ denotes the cross-spectrum between the two pressure signals, $\Phi_{p_i,p_i}(\eta_z,f)$ is the auto-spectrum of each individual signal, and η_z is the spanwise separation distance between the transducers.

Figure 8 shows the line-plots and contour-maps of the lateral coherence measured between the spanwise microphones p1 and p2, with a separation distance of $\eta_z/D = 0.68$ at different angular (θ) positions. Results indicate that at all angles around the cylinder, the maximum lateral coherence occurs at the fundamental shedding frequency and its harmonics (i.e. f_1 and f_2). Moreover, in all cases, except $\theta > 170°$, the lateral coherence value at the fundamental frequency is greater than those at

f_1 and f_2. For $\theta > 170°$, the lateral coherence is dominated by the tonal component at f_1, while the coherence values at f_0 and f_2 reduce to nearly zero. The coherence results at $\theta = 0°$ show a rather broadband behavior, *i.e.* with no sign of distinct tones behavior at f_0, f_1 and f_2. At $\theta = 180°$, the coherence is purely tonal, with a dominant peak at f_1. In the case of the 1st harmonic (f_1), the coherence value at small angles ($\theta < 30°$, *i.e.* within the stagnation and the onset of the laminar boundary layer) is very small and close to the broadband level, but then increases gradually with the angle. Similarly, the coherence at the 2nd harmonic becomes more tonal at the angles larger than 30°, but then rapidly decreases at large angles ($\theta > 130°$), see Fig 8-c. The results presented in Fig. 8 are summarized in Fig. 9, by extracting the peak coherence values measured at the fundamental frequency (f_0) and its harmonics (f_1 and f_2) at different angular positions. As can be observed, the lateral coherence for f_0 is very small at $\theta = 0°$ but increases quickly to one by $\theta = 20°$ and remains almost fully coherent ($\gamma^2_{p_1,p_2} \approx 1$) up to $\theta = 140°$. The f_0 spanwise coherence amplitude then reduces gradually to 0.6 at 175° and ultimately zero at 180°. The spanwise coherence at the f_1 and f_2 frequencies is found to be low at small angles, increasing gradually and reaching their maximum value at about $\theta = 40°$ to 60°, respectively. The peak value for the 1st harmonic (f_1) then varies between 0.6 and 0.8 between $\theta = 60°$ to 180°, while that for the f_2 harmonic drops with θ and reaches zero at $\theta = 180°$.

As discussed above, the results presented in Figs. 8 and 9 were obtained using two pressure transducers with a fixed spanwise separation distance of $\eta_z/D = 0.68$. Figure 10 shows the lateral coherence results for several spanwise spacings and can provide some useful information about the broadband content of the coherent flow structures formed around the cylinder and the length-scale of the structures at different frequencies. Results are presented for the lateral spacings in the range of $\eta_z/D = 0.41$ to 5.95, which should be sufficient for capturing the two- and three-dimensional flow structures. It can be generally seen that the spanwise coherence level between the transducers decreases with η_z/D at all angles. The more interesting issue, however, is that, in addition to the distinct strong

peaks at f_0, f_1 and f_2, the coherence for small lateral spacings of up to $\eta_z/D = 0.68$ has a relatively strong broadband content. However, with increasing the spacing, the lateral coherence becomes entirely tonal and reaches zero at other frequencies. This indicates that the three-dimensional flow structures lose their coherence within a short lateral distance (within $\eta_z/D = 0.68 - 2.6$), while the two-dimensional structures, *i.e.* vortex shedding structures, retain their coherence over a much longer spanwise distance. The coherence results at the stagnation point ($\theta = 0°$) show a broadband behavior with only a tonal peak at the f_0 frequency, indicating that the lift fluctuations can be realized at the stagnation point. Progressing downstream, the strongest broadband coherence occurs at $\theta = 45°$, which can be due to the growing laminar boundary layer and development of larger flow structures. However, at the angles of $\theta = 90°$ and $\theta = 135°$, which correspond to the post-separation regions and turbulent flow, the broadband coherence decreases gradually and approaches zero at 180°. One interesting phenomenon observed here is the emergence of a double-peak coherence behavior near f_0 ($St \approx 0.2$) for the post-separation angles, between $\theta = 90°$ and 135°, with a spanwise characteristic length of between $\eta_z/D = 2.6$ and 4.54, which indicates the emergence of some new large coherent structures near the fundamental tone. This characteristic length is longer than the three-dimensional turbulence structures, but shorter than the two-dimensional vortex shedding structures at the fundamental frequency. The nature of this double-peak phenomenon is not quite clear and requires further investigation. As seen previously in Figs. 8 and 9, the spanwise coherence at $\theta = 180°$ is nearly zero over the entire frequency range and for all lateral distances, except at the f_1-harmonic.

The spanwise coherence results can also be presented in terms of the separation distance (η_z) with the aim to calculate the spanwise length-scales of the structures at different frequencies. Figure 11 presents the coherence between the microphones distributed in the spanwise direction at the fundamental shedding and the 1st and 2nd harmonics at different angular positions. The plot shows that in all cases the coherence level decays uniformly with the separation distance (η_z/D). As expected, the

coherence is approximately one for small separation distances as the two fluctuating pressure signals are perfectly correlated. The coherence level and the decay rate of the coherence of the surface pressure fluctuations along the span of the cylinder can be described by an equivalent correlation length L_c. The correlation length is commonly defined as the spanwise distance over which the coherence drops to 0.5 [38]. In order to find the equivalent correlation length (L_c), the experimental data are fitted with a Gaussian function, i.e. $exp(-a(\eta_z/D)^2)$, where a is the exponents constant and determines the coherence decay rate. Although Gaussian data-fitting is a very common approach, the use of Laplacian data-fitting for modelling of the coherence decay rate has also been reported in the literature [16]. The results in Fig. 11 show that the Gaussian function fits well with the coherence data at the vortex shedding frequency and its harmonics at all angels. It is clear from the results that at the fundamental vortex shedding frequency, the surface pressure remains highly coherent over a long distance along the span of the cylinder (Fig. 11-a), while for the first (Fig. 11-b) and the second harmonics (Fig. 11-c) the coherence decay occurs much faster and over a much shorter span length. Also, as expected, the spanwise coherence level for the pressure signals at the base of the cylinder ($\theta = 180°$) at the fundamental frequency (f_0) drops much more rapidly compared to $\theta = 45°$, 90° and 135° (within the laminar boundary layer and turbulent region). The results for the first harmonic (f_1) show that the spanwise correlation length is much smaller than that of the fundamental frequency (f_0), but the largest structures are observed from the measurements at $\theta = 180°$. Finally, the general trend of the results for the second harmonic (f_2) are similar to the fundamental frequency (f_0), but with a much higher decay rate and smaller correlation length. The curve-fitting coefficient (a) and the equivalent spanwise correlation length values (L_c) extracted from Fig. 11 are summarized in Tables 2 and 3.

In order to better understand the structure of the flow passing over the cylinder, the frequency dependent spanwise length-scale of the flow structures are studied. The spanwise length-scale can be calculated using the surface pressure fluctuations measured along the span in the frequency domain, as

[39]

$$\Lambda(f) = \int_0^{\infty} \sqrt{\gamma^2_{p_i,p_j}(f,\eta_z)}\, d\Delta z \qquad (2)$$

The frequency dependent spanwise length-scale results at different angels are presented in Fig. 12. The results for $\theta = 45°$, $90°$ and $135°$, show similar trends with distinct tonal peaks at the fundamental vortex shedding frequency (f_0) and its harmonics f_1 and f_2. The value of the spanwise length-scale at the fundamental frequency for $\theta = 45°$ reaches about $\Lambda(f_0) = 8.1D$, while that for the 1st and 2nd harmonics are, respectively, $\Lambda(f_1) = 3.6D$ and $\Lambda(f_2) = 2.5D$. These values for the flow structures at $\theta = 90°$ and $135°$, are slightly less than those $45°$, with much smaller values of length-scale at other frequencies, indicating the emergence of more three-dimensional flow structures. Another interesting result here is the appearance of a small tonal peak before the fundamental frequency in the case of $\theta = 90°$ and $135°$, similar to the results in Fig. 10, which shows the emergence of a turbulent structure with a slightly different shedding frequency than that of the main vortex shedding structure and a smaller length-scale of about $3.5D$. The results presented here can be of great use for the development of new CFD-based aeroacoustic models for the calculation of noise from bluff bodies.

3.3.2. Peripheral Coherence

The results in Figs. 8 to 12 show the peripheral coherence of the flow structures as they travel over the cylinder. While the lateral coherence can provide useful information on the spanwise extend of the coherent flow structures, studying the coherence of the pressure signals at different polar locations on the cylinder may give some insight into the evolution of the flow structures as they travel over the cylinder from the stagnation point, to the onset of the laminar boundary layer, to the separation point and into the wake region. Figure 13 shows the changes in the peripheral coherence measured between the circumferential pressure transducers p1, p9, p10, p14 and p15, with 45^o angular spacings. As expected, the pressure signals collected within the laminar and turbulent boundary layers, i.e. pre- and

post-separation locations ($p_{45°} - p_{90°}, p_{45°} - p_{135°}, p_{90°} - p_{135°}$), have the highest level of coherence, while those made with respect to the impingement point ($\theta = 0°$) and the base pressure ($\theta = 180°$) have the lowest level of coherence. The coherence results obtained between the 45°, 90°, and 135° pressure transducers, have strong broadband content, as well as distinct peaks at the fundamental and harmonic frequencies. The coherence results obtained with respect to the $\theta = 0°$ pressure transducer show only tonal components at the fundamental and first harmonic and are nearly zero at all other frequencies. This, of course, makes sense as the broadband components, due to the boundary layer and wake flow structures generated around the cylinder, only have local effects, while the vortex shedding tonal components, can propagate upstream as a hydrodynamic field and reach the $\theta = 0°$ pressure transducer. As a result, in the coherence data measured with respect to the $\theta = 0°$ location, the f_0 and f_1 peaks can be seen clearly. The $90° - 180°$ coherence is also purely tonal, with the coherence at f_1 much stronger than that at f_0, unlike the other cases. Finally, the lowest coherence has been observed between the $\theta = 0°$ and $\theta = 180°$ locations, with the coherence level of only 0.2 at f_0 and f_1.

3.3.3. Surface Pressure Autocorrelation

The autocorrelation of the dynamic pressure data collected at different peripheral locations can provide information about the time-scales of the flow structures responsible for the most energetic pressure fluctuations. The pressure can be found from

$$R_{p,p}(\theta) = \frac{\overline{p(\theta,t)p(\theta,t+\tau)}}{p_{rms}^2(\theta)} \tag{3}$$

where p_{rms} is the root-mean-square of the pressure signal and τ denotes the time delay. The surface pressure autocorrelation results are presented in Fig. 14 for a selected number of angles over a long period of non-dimensional time ($\tau U_\infty / D$). Results have been obtained for the pressure signals collected at $Re = 30 \times 10^3$. The autocorrelation results are presented as solid lines and the dashed lines show the decay rate of the autocorrelation envelop and are based on the Laplacian distribution function,

exp($-b(|\tau|U_\infty/D)$), where b signifies the decay rate. The results for the stagnation point ($\theta = 0°$) shows a relatively rapid decay within $-20 < \tau U_\infty/D < 20$ and very weak oscillation about the mean autocorrelation line. At $\theta = 5°$, the results show some signs of weak oscillations, but decaying fast with time. The oscillations correspond to $St \approx 0.2$, close to the fundamental vortex shedding frequency. The autocorrelation amplitude increases significantly for angles greater than $\theta = 10°$ and peaks at about $45°$. The autocorrelation decay rate increases between $\theta = 45°$ and $90°$. The decay rate (b) remains almost constant within $90°$ to $170°$ and then experiences a rapid decay and a switch in the coherence periodicity to the first vortex shedding harmonic $f_1 = 2f_0$. The contour plot results also show some changes to the data periodicity at $\theta = 45°$ and $135°$. This is believed to be due to some flow transition processes occurring in these two locations, but the underlying physics of these changes is not yet well understood and requires further research.

4. CONCLUSION

A comprehensive study of the surface pressure fluctuations acting on a cylinder in a cross-flow in the subcritical region has been presented. A highly instrumented test rig was designed and built to enable the work. The surface pressure power spectral density results have been presented for different peripheral angles, showing the variations in the dominance of the fundamental vortex shedding frequency and its harmonics in different flow regimes over the cylinder. Results have shown that the fundamental vortex shedding frequency and the second harmonic, characteristic of the cylinder lift fluctuations, peak at around the flow separation angle, while the first harmonic peaks at the base of the cylinder. The lateral coherence studies have also been performed to study the extend of the two-dimensionality of the vortex shedding structures along the span of the cylinder. Results have shown that the structures responsible for the vortex shedding can retain their coherence along the span for about 8 diameters at the fundamental frequency and 3.6 and 2.5 at the first and second harmonics. A secondary

vortex structure has been identified at a frequency slightly lower than the fundamental vortex shedding frequency, with a spanwise characteristic length of about 3.5D. The results in this paper have shown that there is still a need for more fundamental research on the aerodynamics of round cylinders, especially in the context of noise generation mechanism. This experimental work can also provide the impetus for more high-quality computational research on the aerodynamics and aeroacoustics of bluff bodies.

NOMENCLATURE

B	Wind tunnel blockage ratio
C_p	Surface pressure coefficient
C_{p_b}	Base pressure coefficient
D	Cylinder diameter, m
f	Frequency, Hz
f_0	Fundamental vortex shedding frequency, Hz
f_1	First vortex shedding harmonic, Hz
f_2	Second vortex shedding harmonic, Hz
f_s	Sampling frequency, Hz
L_c	Equivalent coherence length, m
N_r	Number of sample records
p	Pressure fluctuations, Pa
PSD	Power Spectral Density
$R_{p,p}$	Surface pressure autocorrelation
Re	Reynolds number, $U_\infty D/v$
St	Strouhal number, fD/U_∞
U_∞	Freestream velocity, m/s
t	Time, s
x,y,z	Coordinate system
$\gamma^2_{p_i,p_j}$	Coherence function
η_z	Spanwise microphone separation distance, m
θ	Peripheral angle, deg
θ_m	Angular position of minimum pressure, deg
θ_s	Separation angle, deg
Λ	Spanwise length scale, m
τ	Time delay, s
ϕ_{pp}	Surface pressure power spectral density, Pa^2/Hz
Φ_{p_i,p_j}	Surface pressure cross-spectrum, Pa^2/Hz

Φ_{p_i,p_i} Surface pressure auto-spectrum, Pa^2/Hz

REFERENCES

[1] Gerrard, J. H., 1955, "Measurements of the Sound from Circular Cylinders in an Air Stream," Proc. Phys. Soc. B, **68**(7), pp. 453-461.

[2] Zdravkovich, M. M., 1997, "Flow around circular cylinder, Volume 1", Oxford University Press.

[3] Strouhal, V., 1878, "Uebereine besondere art der tonenegung," Annalen der Physik und Chemie (Leipzig) Series, **5**(3), pp. 216-251.

[4] Von Karman T., and Rubach, H., 1912, "Uber den mechanismus des flussigkeits- und luftwiderstandes," Physikalische Zeitschrift, **13**, pp. 49-59

[5] Rayleigh, L., 1915, "Aeolian tones," Philosophical Magazine, **29**, pp. 434-444.

[6] Stowell, E. Z., and Deming, A. F., 1936, "Vortex noise from rotating cylindrical rods," Journal of the Acoustical Society of America, **7**(3), pp. 190-198.

[7] Kovasznay, L. S. G., 1949, "Hot wire investigation of the wake behind cylinders at low Reynolds numbers," Proceedings of the Royal Society of London Series A, **198**, pp. 174-190.

[8] Roshko, A., 1953, "On the development of turbulent wakes from vortex streets," NACA-TN-2913.

[9] Curle, N., 1955, "The influence of solid boundaries upon aerodynamic sound," Proceedings of the Royal Society of London Series A, **231**, pp. 505-514.

[10] Yudin, E. Y., 1944, "On the vortex sound from rotating rods," Zhurnal Tekhnicheskoi Fiziki, **14**(9), pp. 561.

[11] Blevins, R. D., 1984, "Review of sound induced by vortex shedding from cylinders," Journal of Sound and Vibration **92**(4), pp. 455-470.

[12] Etkin B., and Ribner, H. S., 1958, "Canadian research in aerodynamic noise," University of Toronto, Institute of Astrophysics, UTIA Review. No. 13.

[13] Ffowcs Williams J. E., and Hawkings, J. E., 1968, “Sound generation by turbulence and surfaces in arbitrary motion,” Proceedings of the Royal Society of London Series A, **264**, pp. 321-342.

[14] Oguma, Y., Yamagata, T., Fujisawa, N., 2013, “Measurement of sound source distribution around a circular cylinder in a uniform flow by combined particle image velocimetry and microphone technique,” J. Wind Eng. Ind. Aerodyn. **118**, pp. 1-11.

[15] Schlinker, R. H., Fink, M. R., Amiet, R. K., 1976, “Vortex noise from nonrotating cylinders and airfoils”, AIAA paper. 81.

[16] Casalino, D., Jacob, M., 2003, “Prediction of aerodynamic sound from circular rods via spanwise statistical modeling,” Journal of Sound and Vibration, **262**(4), pp. 815-844.

[17] Fujita, H., Suzuki, H., 2002, “The Aeolian tone and the surface pressure in high Reynolds number flow,” AIAA paper. 99.

[18] Ozkan, G. M., Firat, E., Akilli H., 2017, “Control of Vortex Shedding Using a Screen Attached on the Separation Point of a Circular Cylinder and Its Effect on Drag,” ASME J. Fluids Eng., **139**(7), pp. 1-11.

[19] Ashtiani Abdi, I., Hooman, K., Khashehchi, M., 2014, “A Comparison Between the Separated Flow Structures Near the Wake of a Bare and a Foam-Covered Circular Cylinder,” ASME J. Fluids Eng., **136**(12), pp. 1-8.

[20] Garcia-Sagrado, A., Hynes, T. 2012, "Wall pressure sources near an airfoil trailing edge under turbulent boundary layers," Journal of Fluids and Structures, **30**, pp. 3-34.

[21] Barlow, J.B., Rae, W.H., Pope, A., 1999, “Low-Speed Wind Tunnel Testing,” 3rd edn. Wiley, New York.

[22] Yavuzkurt, S., 1984, “A Guide to Uncertainty Analysis of Hot-Wire Data”, ASME J. Fluids Eng., **106**(2), pp. 181-186.

[23] Wilkins, S. J., Hall, J. W., 2014, “Experimental investigation of a tandem cylinder system with a yawed upstream cylinder,” Journal of Pressure Vessel Technology, **136**(1), pp. 1-8.

[24] Hutcheson, F. V., Brooks, T. F., Lockard, D. P., Choudhari, M. M., and Stead, D. J., 2014, “Acoustics and Surface Pressure Measurements from Tandem Cylinder Configurations”, 20th AIAA/CEAS Aeroacoustics Conference, AIAA AVIATION Forum, 2762.

[25] Corcos, G.M., 1963, “Resolution of pressure in turbulence,” Journal of the Acoustical Society of America **35**(2), pp. 192-199.

[26] Goody, M., 2004, “Empirical spectral model of surface pressure fluctuations,” AIAA Journal, **42**(9), pp. 1788-1794.

[27] Bull, M. K., and Thomas, A. S. W., 1976, “High Frequency Wall-Pressure Fluctuations in Turbulent Boundary Layers,” The Physics of Fluids, **19**(4), pp. 597-599.

[28] Afshari, A., Azarpeyvand M., Dehghan, A. A., Szoke, M., 2016, "Trailing edge noise reduction using novel surface treatments." In 22nd AIAA/CEAS Aeroacoustics Conference, p. 2834.

[29] Goody, M., 1999, "An Experimental Investigation of Pressure Fluctuations in Three-Dimensional Turbulent Boundary Layers," Ph.D. Dissertation, Aerospace Engineering, Virginia Polytechnic Institute and State University.

[30] Goody, M. C., and Roger L. S., 1999, "An experimental investigation of pressure fluctuations in three-dimensional turbulent boundary layers," No. VPI-AOE-268. Virginia Polytechnic Inst. and State Univ. Blacksburg Dept. of Aerospace and Ocean Engineering.

[31] Bendat, J. S., Piersol, A. G., 2011, "Random data: analysis and measurement procedures," (Vol. 729). John Wiley & Sons

[32] West, G. S., Apelt, C. J., 1982, "The effects of tunnel blockage and aspect ratio on the mean flow past a circular cylinder with Reynolds numbers between 104 and 105," J. Fluid Mech., **114**, pp. 361-377.

[33] Weidman, P.D., 1968, "Wake Transition and Blockage Effects on Cylinder Base Pressures" Ph.D. thesis. California Institute of Technology, Pasadena, California.

[34] Fage, A., Falkner, V. M., 1931, "Further experiments on the flow around a circular cylinder" ARC R&M 1369, pp. 1-13.

[35] Sadeh, W., and Saharon, D.B., 1982, "Turbulence Effect On Cross-flow Around a Circular Cylinder at Subcritical Reynolds Numbers," NASA Contractor Report 3622.

[36] Sun, T. F., Gu, Z. F., Hu, D. X., Zhang, L. L., 1992, "Fluctuation pressure on two circular cylinders at high Reynolds numbers, Journal of wind engineering and industrial aerodynamics," **41**(1-3), pp. 577-588.

[37] Gu, F., Wang, J. S., Qiao, X. Q., and Huang, Z., 2012, "Pressure distribution, fluctuating forces and vortex shedding behavior of circular cylinder with rotatable splitter plates." Journal of fluids and structures, **28**, 263-278.

[38] Kato, C., Lida, A., Fujita, H., Ikegawa, M., 1993, "Numerical Prediction of Aerodynamic Noise from Low Mach Number Turbulent Wake", AIAA Paper 145.

[39] Gruber, M., 2012, "Airfoil noise reduction by edge treatments," Ph.D. Thesis, Department of Engineering, University of Southampton.

Figure Captions List

Fig. 1 (a) The geometry of the contraction nozzle and the experimental setup, (b) the sensing area on the cylinder equipped with static pressure taps and spanwise and peripheral pressure transducers.

Fig.2 In-situ boundary layer surface pressure measurement using a pressure transducer installed under a pinhole

Fig.3 Schematic of the calibrator system used for the calibration of the in-situ pressure transducers in the pinhole configuration

Fig.4 Amplitude and phase of the transfer function for a Panasonic WM-61A pressure transducer.

Fig.5 Pressure coefficient at different peripheral locations. Symbols: present study; Lines: prior studies.

Fig.6 Surface pressure power spectral density measured at different angular positions at $Re = 30 \times 10^3$. (a) PSD results for pressure transducers between $\theta = 0^o$ to 90^o, (b) PSD results for pressure transducers between $\theta = 90^o$ to 180^o, (c) Counter map of the surface pressure PSD over the circumference of the cylinder.

Fig.7 Variation of the surface pressure power spectral amplitude at the fundamental vortex shedding frequency (f_0), the first harmonic ($f_1 = 2f_0$) and the second harmonic ($f_2 = 3f_0$). The hollow markers are used when the tones are not visible and the values are taken from the broadband spectra at the selected frequencies.

Fig.8 Lateral coherence measured between two pressure transducers with a separation distance of $\eta_z/D = 0.68$ at different angular position at $Re = 30 \times 10^3$. (a) Lateral coherences

		for $\theta = 0°$ to 90°; (b) Lateral coherences for $\theta = 90°$ to 180°; (c) Contour map of the lateral coherence around the cylinder.
	Fig.9	Amplitude of the coherence between two lateral pressure transducers with the spanwise spacing of $\eta_z/D = 0.68$ at different angular position at $Re = 30 \times 10^3 at$ the fundamental vortex shedding frequency (f_0), the first ($f_1 = 2f_0$) and second ($f_2 = 3f_0$) harmonics.
	Fig.10	Lateral coherence measured between several spanwise locations at different angular positions at $Re = 30 \times 10^3$.
	Fig.11	Lateral coherence measured on a circular cylinder model between spanwise microphones p1 to p8 for $Re = 30 \times 10^3$ at different angular positions. Data are fitted with a Gaussian function ($exp(-a(\eta_z/D)^2)$), shown as the solid lines. (a) Fundamental vortex shedding frequency (f_0), (b) first harmonic (f_1), and (c) second harmonic (f_2).
	Fig. 12	Frequency-dependent spanwise length-scales of the surface pressure fluctuations at different angular position.
	Fig.13	Peripheral coherence measured around the circular cylinder model at $Re = 30 \times 10^3$.
	Fig.14	Autocorrelation coefficient measured at different angular position at $Re = 30 \times 10^3$. Data are fitted with a Laplacian function (dash line) at angels of $\theta = 45°, 90°, 135°$ and 180°. (a) Surface pressure autocorrelation within $\theta = 0°$ to 90° ; (b) Surface pressure autocorrelation within $\theta = 90°$ to 180°; (c) Counter map of the surface pressure autocorrelation coefficient around the cylinder.

Table Caption List

Table 1 Position of pressure pinholes on the surface of model

Table 2 The coherence decay constant (a) found from the curve-fitting of the experimental data with a Gaussian function ($exp(-a(\eta_z/D)^2)$))

Table 3 Non-dimensional equivalent correlation length (L_c/D) found from the curve-fitting of the experimental data with a Gaussian function ($exp(-a(\eta_z/D)^2)$))

Fig.1

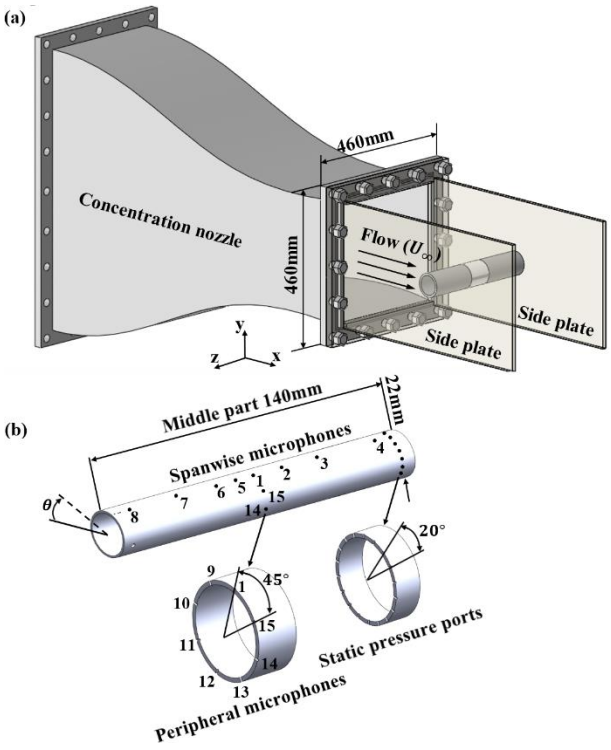
(a)
460mm
Concentration nozzle
460mm
Flow (U_∞)
Side plate
Side plate
y
z
x
(b)
Middle part 140mm
22mm
Spanwise microphones
θ
20°
45°
Static pressure ports
Peripheral microphones

Fig.2

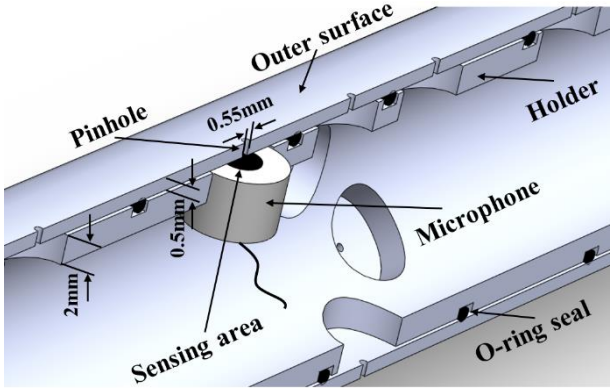
Outer surface
Pinhole
0.55mm
Holder
Microphone
0.5mm
2mm
Sensing area
O-ring seal

Fig.3

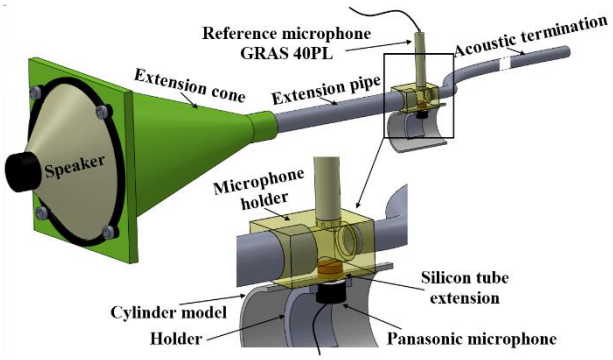
Reference microphone
GRAS 40PL
Acoustic termination
Extension cone
Extension pipe
Speaker
Microphone
holder
Silicon tube
extension
Cylinder model
Holder
Panasonic microphone

Fig.4

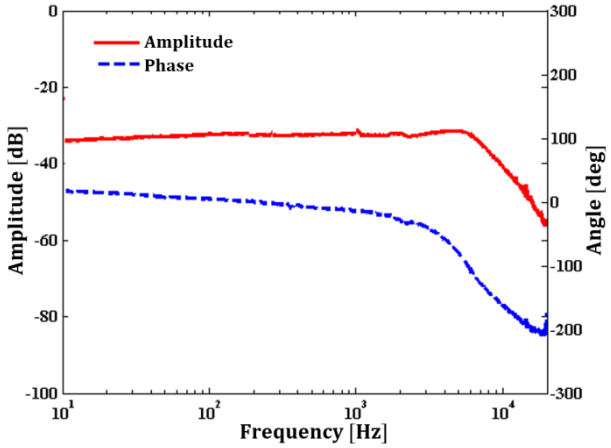
Amplitude
Phase
Amplitude [dB]
Angle [deg]
Frequency [Hz]
0
-20
-40
-60
-80
-100
300
200
100
0
-100
-200
-300
10^1
10^2
10^3
10^4

Fig.5

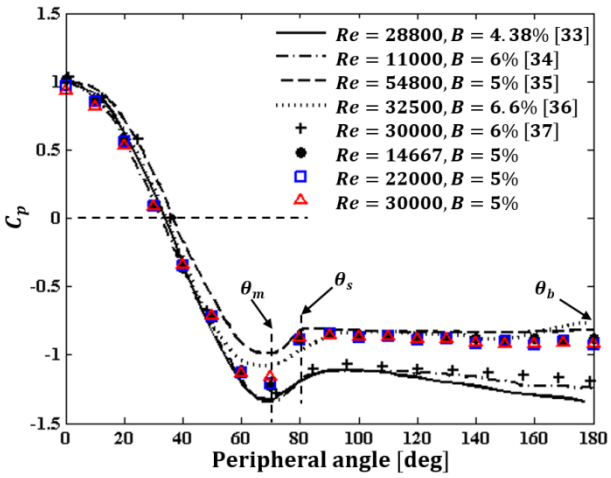
$Re = 28800, B = 4.38\%$ [33]
$Re = 11000, B = 6\%$ [34]
$Re = 54800, B = 5\%$ [35]
$Re = 32500, B = 6.6\%$ [36]
$Re = 30000, B = 6\%$ [37]
$Re = 14667, B = 5\%$
$Re = 22000, B = 5\%$
$Re = 30000, B = 5\%$
C_p
θ_m
θ_s
θ_b
Peripheral angle [deg]

Fig.6

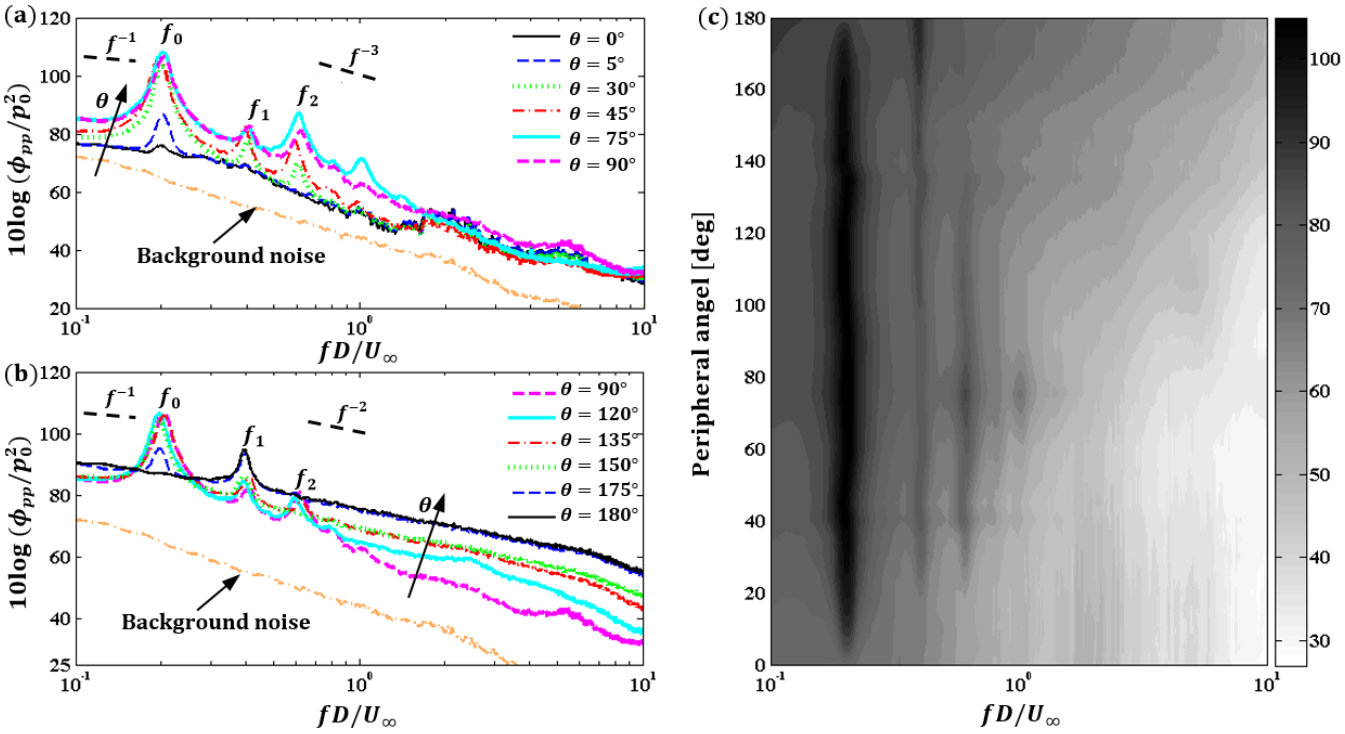
(a)
(b)
(c)
f^{-1}
f_0
f^{-3}
f^{-2}
f_1
f_2
θ
$\theta = 0°$
$\theta = 5°$
$\theta = 30°$
$\theta = 45°$
$\theta = 75°$
$\theta = 90°$
$\theta = 120°$
$\theta = 135°$
$\theta = 150°$
$\theta = 175°$
$\theta = 180°$
Background noise
$10\log(\phi_{pp}/p_0^2)$
fD/U_∞
Peripheral angel [deg]

Fig.7

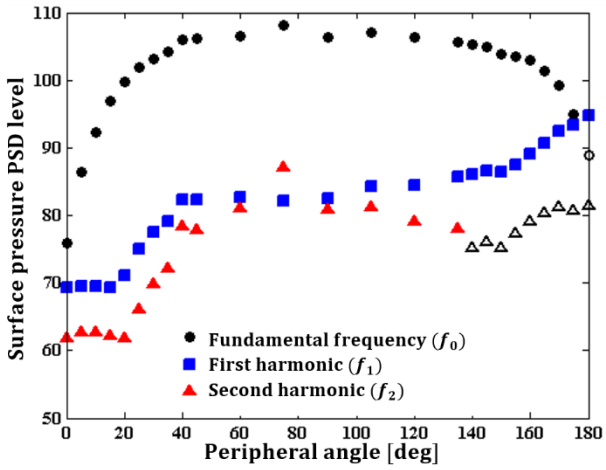
Surface pressure PSD level
Peripheral angle [deg]
Fundamental frequency (f_0)
First harmonic (f_1)
Second harmonic (f_2)
110
100
90
80
70
60
50
0
20
40
60
80
100
120
140
160
180

Fig.8

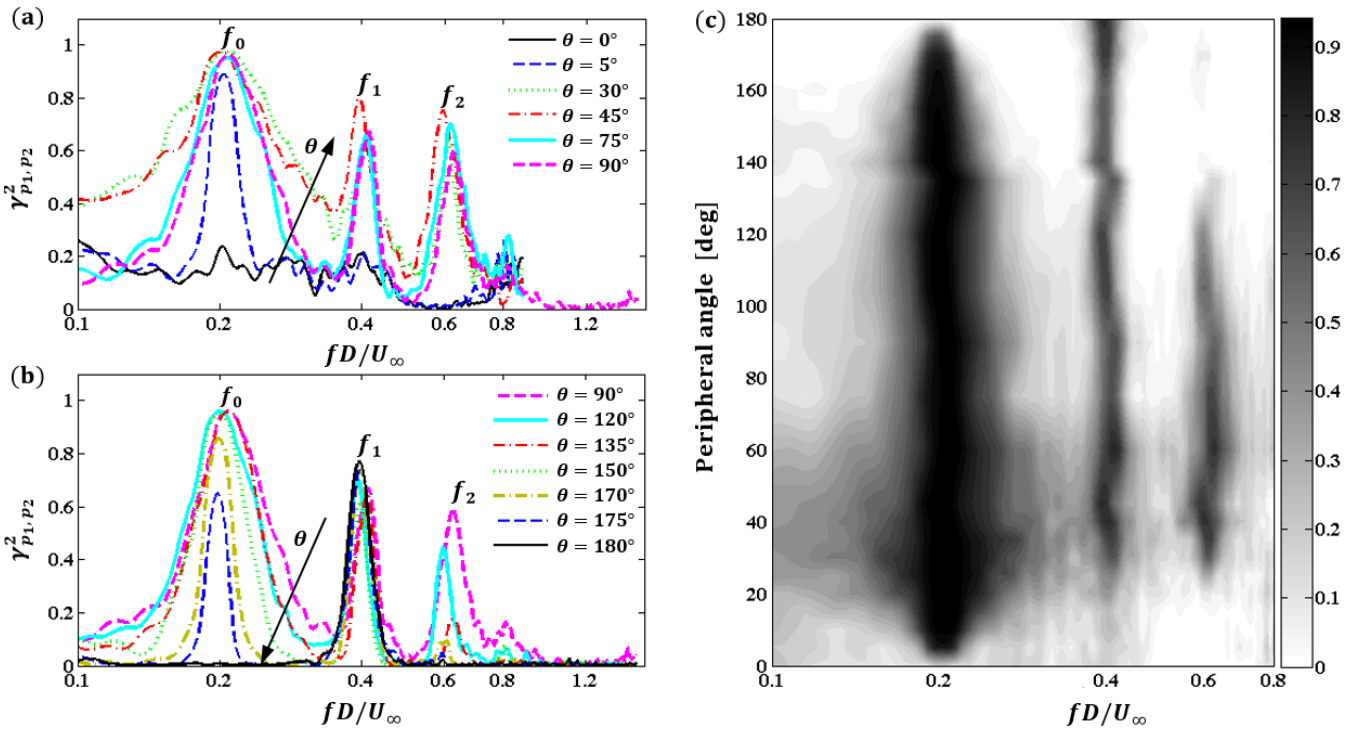
(a)
f_0
f_1
f_2
θ
$\theta = 0°$
$\theta = 5°$
$\theta = 30°$
$\theta = 45°$
$\theta = 75°$
$\theta = 90°$
$\gamma^2_{p_1,p_2}$
fD/U_∞
(b)
f_0
f_1
f_2
θ
$\theta = 90°$
$\theta = 120°$
$\theta = 135°$
$\theta = 150°$
$\theta = 170°$
$\theta = 175°$
$\theta = 180°$
$\gamma^2_{p_1,p_2}$
fD/U_∞
(c)
Peripheral angle [deg]
fD/U_∞

Fig.9

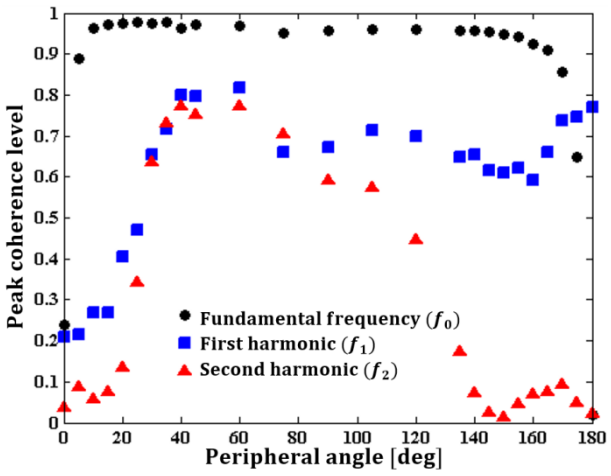
Peak coherence level
Peripheral angle [deg]
Fundamental frequency (f_0)
First harmonic (f_1)
Second harmonic (f_2)
0
0.1
0.2
0.3
0.4
0.5
0.6
0.7
0.8
0.9
1
0
20
40
60
80
100
120
140
160
180

Fig.10

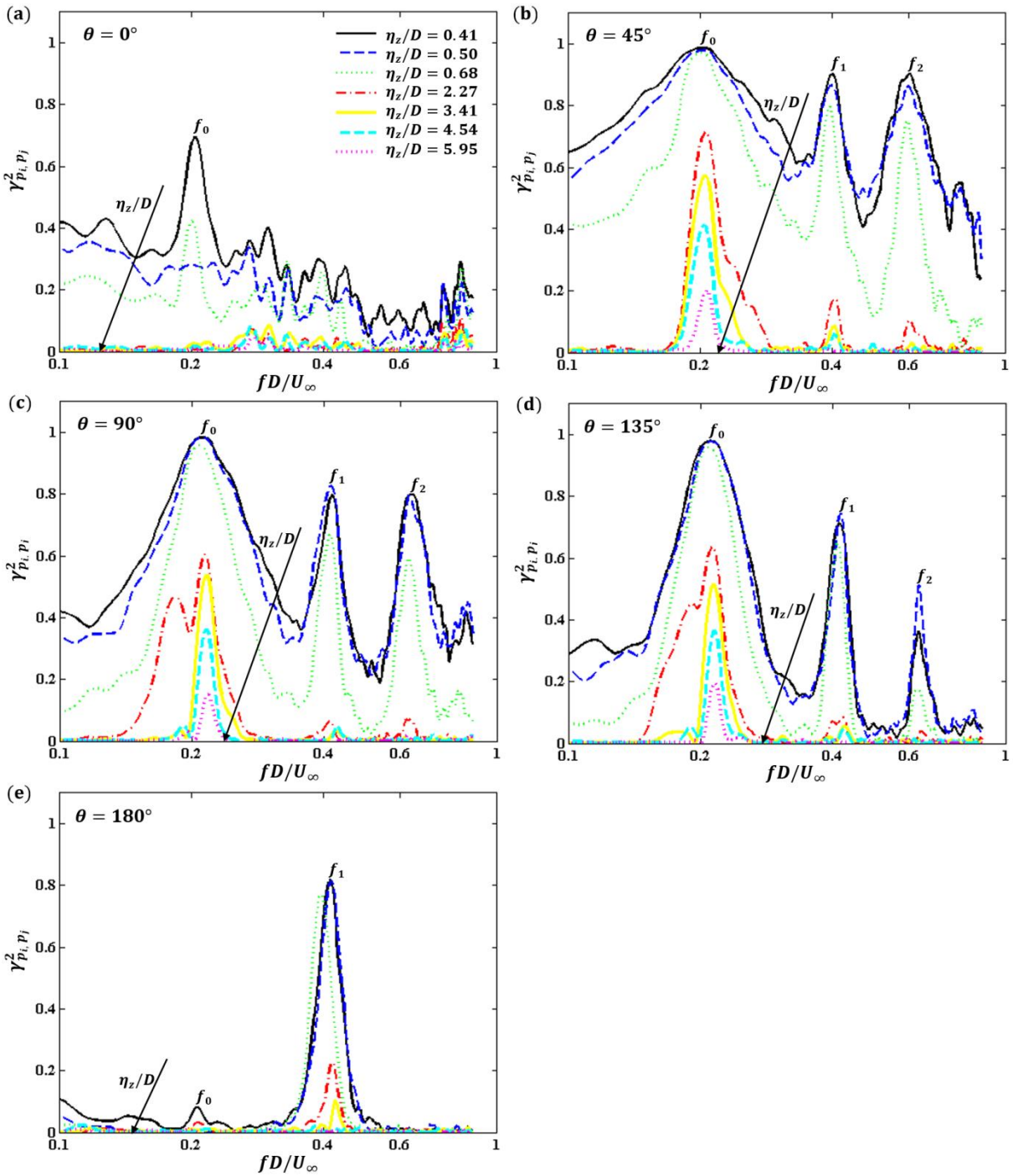
(a)
θ = 0°
η_z/D = 0.41
η_z/D = 0.50
η_z/D = 0.68
η_z/D = 2.27
η_z/D = 3.41
η_z/D = 4.54
η_z/D = 5.95
f_0
η_z/D
γ²_{p_i,p_j}
fD/U_∞
(b)
θ = 45°
f_0
f_1
f_2
η_z/D
(c)
θ = 90°
(d)
θ = 135°
(e)
θ = 180°

Fig.11

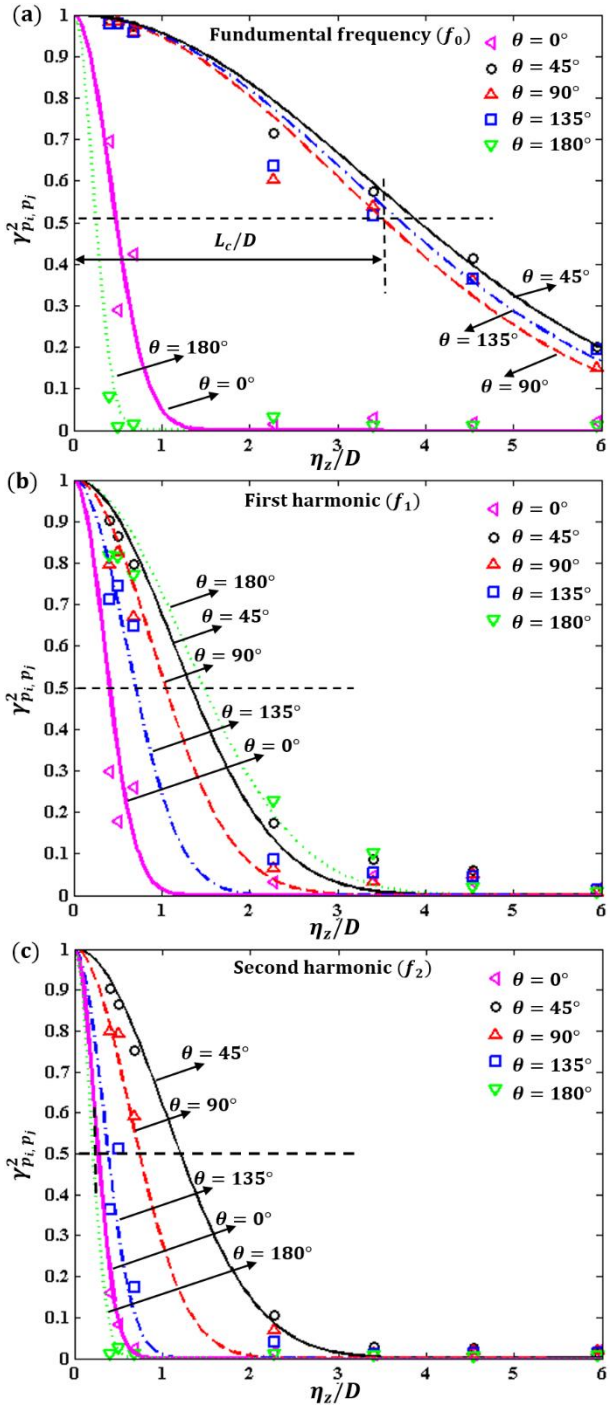
(a)
Fundumental frequency (f_0)
$\theta = 0°$
$\theta = 45°$
$\theta = 90°$
$\theta = 135°$
$\theta = 180°$
L_c/D
$\gamma^2_{p_i,p_j}$
η_z/D
(b)
First harmonic (f_1)
(c)
Second harmonic (f_2)

Fig.12

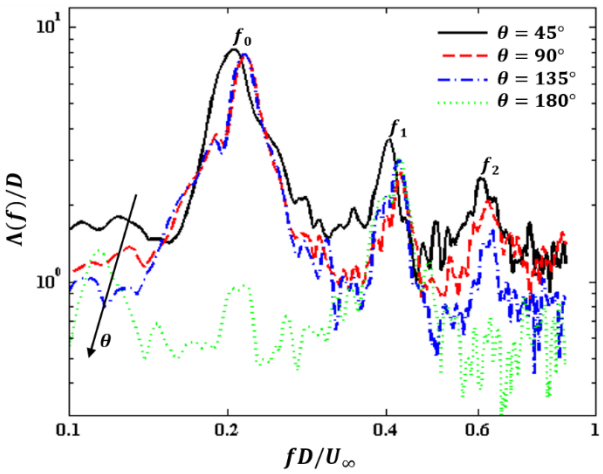
10^1
10^0
$\Lambda(f)/D$
f_0
f_1
f_2
θ
$\theta = 45°$
$\theta = 90°$
$\theta = 135°$
$\theta = 180°$
0.1
0.2
0.4
0.6
1
fD/U_∞

Fig.13

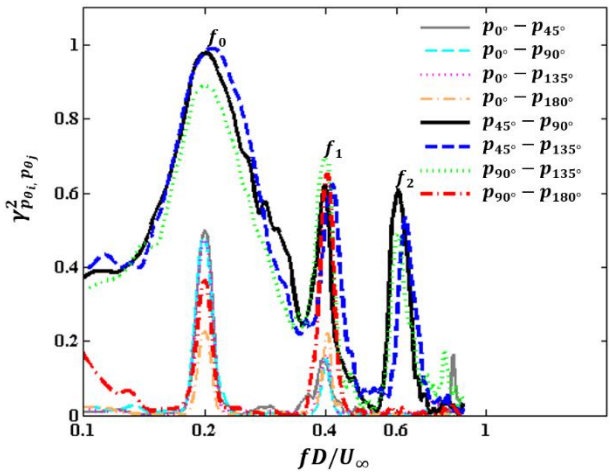
f_0
f_1
f_2
$p_{0°} - p_{45°}$
$p_{0°} - p_{90°}$
$p_{0°} - p_{135°}$
$p_{0°} - p_{180°}$
$p_{45°} - p_{90°}$
$p_{45°} - p_{135°}$
$p_{90°} - p_{135°}$
$p_{90°} - p_{180°}$
$\gamma^2_{p_{0i}, p_{0j}}$
fD/U_∞
0
0.2
0.4
0.6
0.8
1
0.1
0.2
0.4
0.6
1

Fig. 14

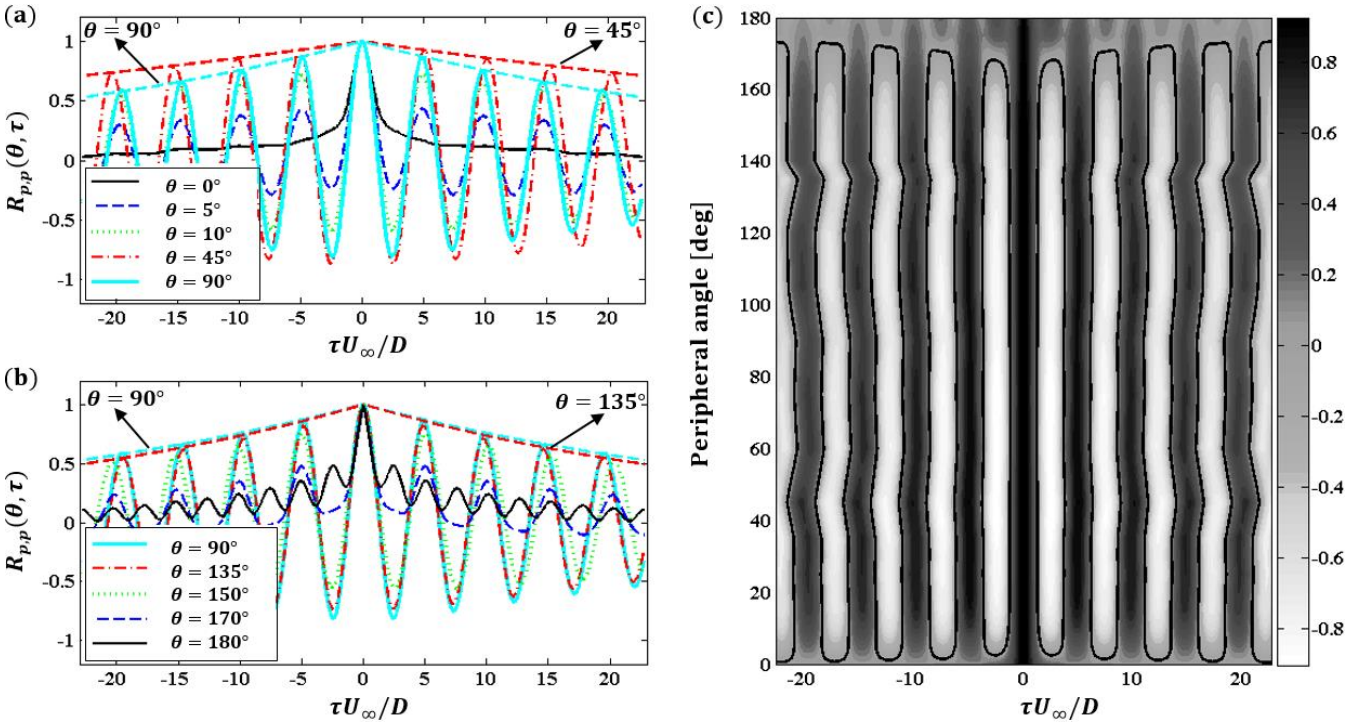
(a)
θ = 90°
θ = 45°
θ = 0°
θ = 5°
θ = 10°
θ = 45°
θ = 90°
$R_{p,p}(\theta,\tau)$
$\tau U_\infty/D$
(b)
θ = 90°
θ = 135°
θ = 90°
θ = 135°
θ = 150°
θ = 170°
θ = 180°
$R_{p,p}(\theta,\tau)$
$\tau U_\infty/D$
(c)
Peripheral angle [deg]
$\tau U_\infty/D$

Table 1

Microphones	z/D	$\boldsymbol{\theta}$ (deg)	Microphones	z/D	$\boldsymbol{\theta}$ (deg)
p1	0.0	90	p9	0.282	45
p2	0.682	90	p10	0.0	0.0
p3	1.545	90	p11	0.282	-45
p4	2.955	90	p12	0.0	-90
p5	-0.41	90	p13	0.282	-135
p6	-0.91	90	p14	0.0	180
p7	-1.864	90	p15	0.282	135
p8	-3.0	90	----	----	----

Table 2

	$\boldsymbol{\theta = 0°}$	$\boldsymbol{\theta = 45°}$	$\boldsymbol{\theta = 90°}$	$\boldsymbol{\theta = 135°}$	$\boldsymbol{\theta = 180°}$
Fundamental Peak ($\boldsymbol{f_0}$)	3.0	0.05	0.06	0.07	11
First harmonic ($\boldsymbol{f_1}$)	4.5	0.40	0.60	1.20	0.3
Second harmonic ($\boldsymbol{f_2}$)	8.0	0.50	1.00	5.00	14

Table 3

	$\boldsymbol{\theta = 0°}$	$\boldsymbol{\theta = 45°}$	$\boldsymbol{\theta = 90°}$	$\boldsymbol{\theta = 135°}$	$\boldsymbol{\theta = 180°}$
Fundamental Peak ($\boldsymbol{f_0}$)	0.48	3.72	3.36	3.13	0.25
First harmonic ($\boldsymbol{f_1}$)	0.40	1.31	1.07	0.75	1.50
Second harmonic ($\boldsymbol{f_2}$)	0.29	1.18	0.83	0.38	0.21